Analysis of a Large Rock Slope Failure on the East Wall of the LAB Chrysotile Mine in Canada: LiDAR Monitoring and Displacement Analysis

Caudal P & Grenon M
Faculté des sciences et de génie, Département de génie des mines, de la métallurgie et des matériaux, Université Laval, Québec, Canada

Turmel D & Locat J
Faculté des sciences et de génie, Département de géologie et génie géologique, Université Laval, Québec, Canada

ABSTRACT
A major mining slope failure occurred in July 2012 on the East wall of the LAB Chrysotile mine in Canada. The major consequence of this failure was the loss of the local highway (Road 112), the main economic link between the region and the Northeast USA. This paper is part of a proposed integrated remote sensing–numerical modelling methodology to analyze mining rock slope stability. This paper presents the Light Detection and Ranging (LiDAR) monitoring of this slope failure. The main focus is the investigation of that rock slide using both terrestrial (TLS) and airborne (ALS) LiDAR scanning. Since 2010, four ALS and 14 TLS were performed to characterize and monitor the slide. First, laser scanning was used to investigate the geometry of the slide. The failure zone was 1100 m by 250 m in size with a mobilized volume of 25 hm^3. Laser scanning was then used to investigate the rock slide's 3D displacement, thereby enabling a better understanding of the sliding kinematics. The results clearly demonstrate the ability of the proposed approach to monitor and quantify large-scale rock mass failure. The slope was monitored for a period of 5 years, and the total displacement was measured at every survey. The maximum cumulative total displacement reached was 145 m. This paper clearly shows the ability of LiDAR scanning to provide valuable quantitative information on large rock mass failures involving very large displacements.

KEYWORDS
Open pit mining, Slope stability, LiDAR monitoring, Case study, Slope change monitoring, Very large slope displacements

CITATION
Caudal, P., Grenon, M., Turmel, D., & Locat, J. (2017). Analysis of a Large Rock Slope Failure on the East Wall of the LAB Chrysotile Mine in Canada: LiDAR Monitoring and Displacement Analyses. Rock Mechanics and Rock Engineering, 50(4), 807-824. doi:10.1007/s00603-016-1145-3

This is the author's version of the original manuscript.
The final publication is available at Springer Link Online via https://link.springer.com/article/10.1007/s00603-016-1145-3

1 INTRODUCTION

Designing mining rock slopes is very different from designing rock slopes in civil engineering. As Bye and Bell (2001) state, in order to minimize the amount of waste rock that has to be removed in the recovery of an ore body, the ultimate slopes of an open pit mine generally are excavated to the steepest possible angle. Unfortunately, the economic benefits gained can be negated by major slope failure. Consequently, continual evaluation of the stability of the ultimate pit slopes is vital. Combining slope monitoring and numerical modelling is thus a critical feature of mining rock slope engineering; stability is thereby optimized, and instabilities can be managed during and after the mining operation period.

Several tools and methods have been proposed and used over the years to perform qualitative or quantitative surface and subsurface monitoring. As mentioned by Read and Stacey (2009) among others, all have their place in specific mine environments, and they are often related to the potential failure size. Several numerical methods have also been proposed over the years to perform prospective and retrospective slope stability analysis.

As stated by Michoud et al. (2010), the most recent advances in our ability to detect rock slope instabilities across a wide range of spatial and temporal scales have come from applying terrestrial, airborne, and spaceborne remote sensing techniques; these remote sensing techniques rely on photogrammetry, synthetic aperture radar methods (InSAR, GB-SAR) and Light Detection and Ranging (LiDAR). The last 5–10 years have seen the production of an important body of scientific literature on using these methods on natural rock slopes, some of the most recent studies being Curtaz et al. (2014), Caduff et al. (2015), Lato et al. (2014) and Abella´n et al. (2014). However, there is far less scientific literature on rock slope monitoring for open pit mining applications, thus limiting its optimal usage in that context, Eberhardt and Stead (2011), Woo et al. (2012), Dick et al. (2014). What is more, the literature is often concerned with small-scale displacements and rarely focuses on decameter-scale slope displacements.

A major mining slope failure characterized by large ground movement occurred in July 2012 on the East wall of the LAB Chrysotile mine in Canada after the mine closure. No data from ‘‘conventional’’ instrumentation was available at the mine site to quantify slope instability around the time of the major slope failure. This paper is part of an integrated remote sensing—numerical modelling approach to analyze mining rock slope stability. More specifically, the study’s main objective was to establish a working methodology—combining remote sensing and numerical modelling—for the analysis of such a slope failure in a mining environment where conventional monitoring data are limited and very large displacements are observed, and thus better understand the mechanism involved at the time of slope failure. This can be useful at every stage of the mining cycle, from start up to after mine closure, as well as for abandoned mines.

The accompanying paper, Grenon et al. (2016), focuses on using numerical modelling to back-analyze the major failure. The present paper presents the LiDAR monitoring results of this slope failure. The paper’s main focus is the investigation of that rock slide using both terrestrial (TLS) and airborne (ALS) laser scanning. First of all, laser scanning was used to investigate the geometry of the slide, its volume, topography, size and orientation of the scarp, and the rise in the pit water level. It was then used to investigate the rock slide’s 3D displacement, thus enabling a better understanding of the sliding kinematics. The displacement analysis presented is based on point clouds comparison, enabling quantitative displacement maps to be created. This paper also gives the limitations of the approach being used.

2 CASE STUDY

The Road 112 is the most important public highway in the region, acting as the major commercial link between the region and the Northeast USA. This road was located immediately adjacent to the crest of the East wall of the LAB Chrysotile mine (Fig. 1). In July 2012, a major slope failure occurred on the East wall of the pit, taking with it a large portion of Road 112 (Fig. 1). During this failure, a vertical movement of 70 m was observed. The lateral extent of the failure was 1.1 km. This case study is of singular interest because of the following features: as the accompanying paper, Grenon et al. (2016) makes clear, the previous mining operations and the rise of the water level in the pit played an important role in the magnitude and timing of the slope failure; a very large displacement occurred, and the failure was active for a long period of time; and governmental authorities were concerned about a potential landslide-generated tsunami that would affect the town of Thetford Mines adjacent to the pit, Turmel et al. (2015). As the pit was not in operation at the time of failure, no conventional monitoring devices were in operation, and it was not possible to install them because access to the site was difficult. For all those reasons, LiDAR monitoring could provide invaluable quantitative information to help our understanding of the failure mechanisms involved.

2.1 Mine History

During the last century, the Chaudière-Appalaches region, in southern Québec, Canada, was a major world producer of asbestos, the source of the region’s wealth. Nowadays, no asbestos mines are in operation in Quebec. Nevertheless, mine residues in the form of large open pits and their associated tailings characterize the region’s landscape.

Before 1953, a 2.8-km-long lake (Black Lake) with an average depth of 15 m was located at the present LAB Chrysotile site. Dredging operations started in 1955 to remove the layer of mud (average thickness of 30 m) and to remove the lake and the associated river. Road 112 (white line in Fig. 1) was moved to this location before a major mining pushback in the 1970’s. A railway, built before mining operations started in 1958, was also observed east of the road. The final, larger pit was approximately 320 m deep, with a diameter ranging from 1.5 to 1.8 km. A smaller pit (the Northeast extension) with a diameter ranging between 0.625 and 0.550 km was also mined adjacent to this large pit.

2.2 Geology of the Mining Site

The geology of the LAB Chrysotile mine site is complex. The lithology of the site includes mainly peridotite and serpentinite, but also granite and talc. The simplified geological map adapted from Beauchamp (1994) provided a general representation of the lithological domains, (Fig. 1). The four main types of rock found at the site are schistose serpentinite (in green), peridotite (in purple), granite (in blue) and a talc-carbonate shear zone (in brown).

As shown in Fig. 1, the peridotite is located on the upper part of the East wall. Apart from the talc-carbonate shear zone, the schistose serpentinite constitutes the most important volume of rock mass in the main pit. It is important to note that a granite dyke crosses the mine site in a northeast–southwest direction. It physically defines the limit between the main pit and the NE extension.

2.3 Brief History of Recent Slope Instabilities on the East Wall of the Main Pit

The first signs of instability were observed on the ground near the roadway in the fall of 2008. A first slide occurred the night of August 11, 2009. It was 60 m long and 90 m wide. The head of the sliding zone was located less than 6 m from Road 112’s paved shoulder (Fig. 2). Following this failure, monitoring of the sector showed the emergence of open fractures more than 25 mm wide and 0.80 m deep between the failure zone and the southern end of the roadway area. Consequently, while awaiting a new road layout on the West wall of the pit (Fig. 1), the Ministère des Transports du Quéebec (MTQ) decided to temporarily displace Road 112 on the railway line east of it, so as to move it away from the slide edges (temporary road in Fig. 1). During the week of October 12, 2009, new cracks were observed 500 m south of the location of the August failure;

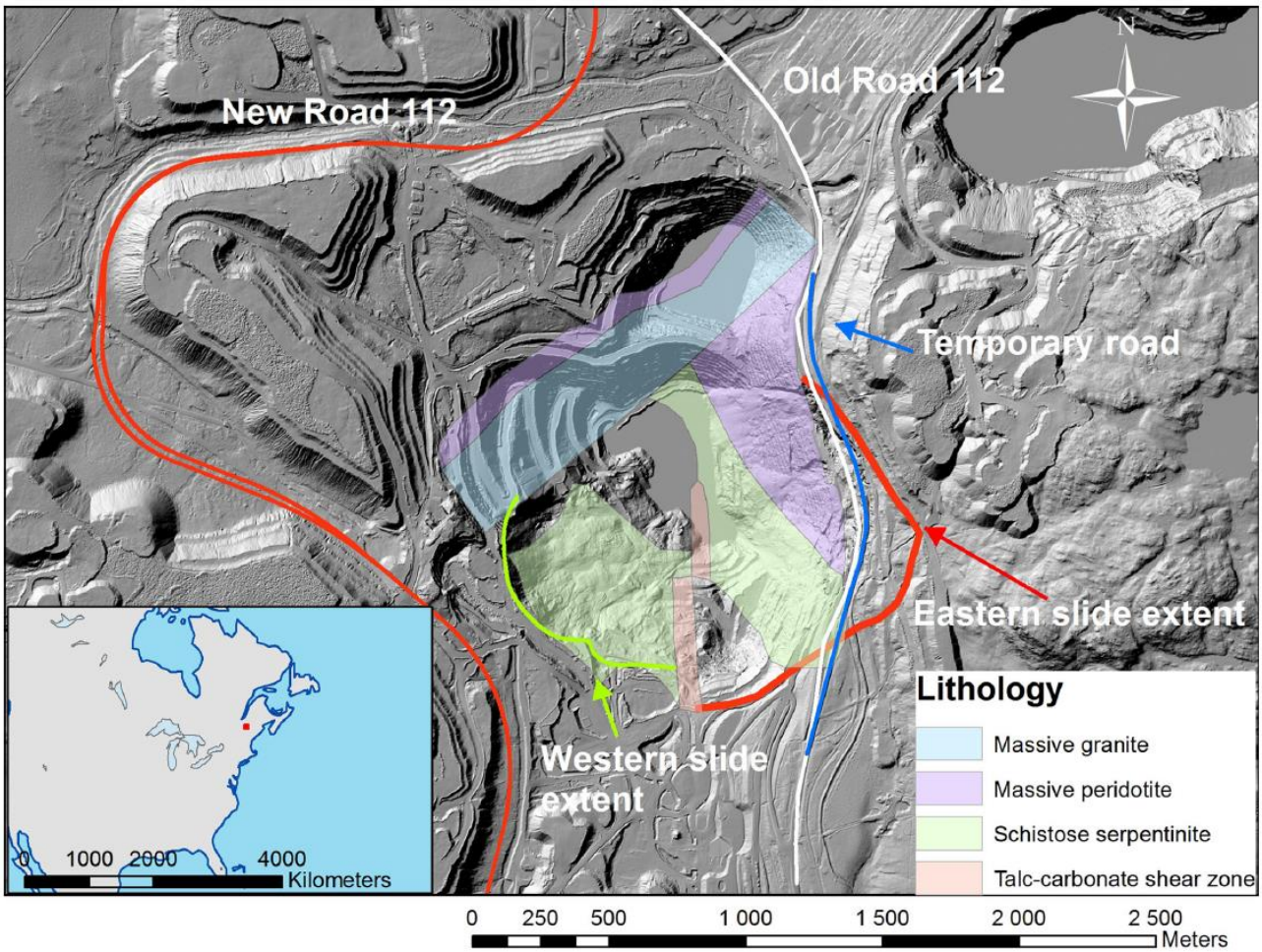

Figure 1. Location of the LAB Chrysotile mine and surrounding road infrastructures shown in conjunction with mine lithology adapted from Beauchamp (1994)

Figure 2. Early signs of failure on the evening of August 11, 2009

the Road 112 shoulder guardrail was deformed in this same area.

In the spring of 2010, the cracks widened and the signs of subsidence increased, revealing the outlines of instability toward the north of Road 112, close to an observation tower. Also, although the guardrail had been fixed the previous year, it became deformed again south of the East wall. Other cracks in the ditches along Road 112 were observed up until May 2010. The ditch of the temporary road (on the former railway line) on the side of the mine had an open fracture on the surface, 0.15–0.20 m

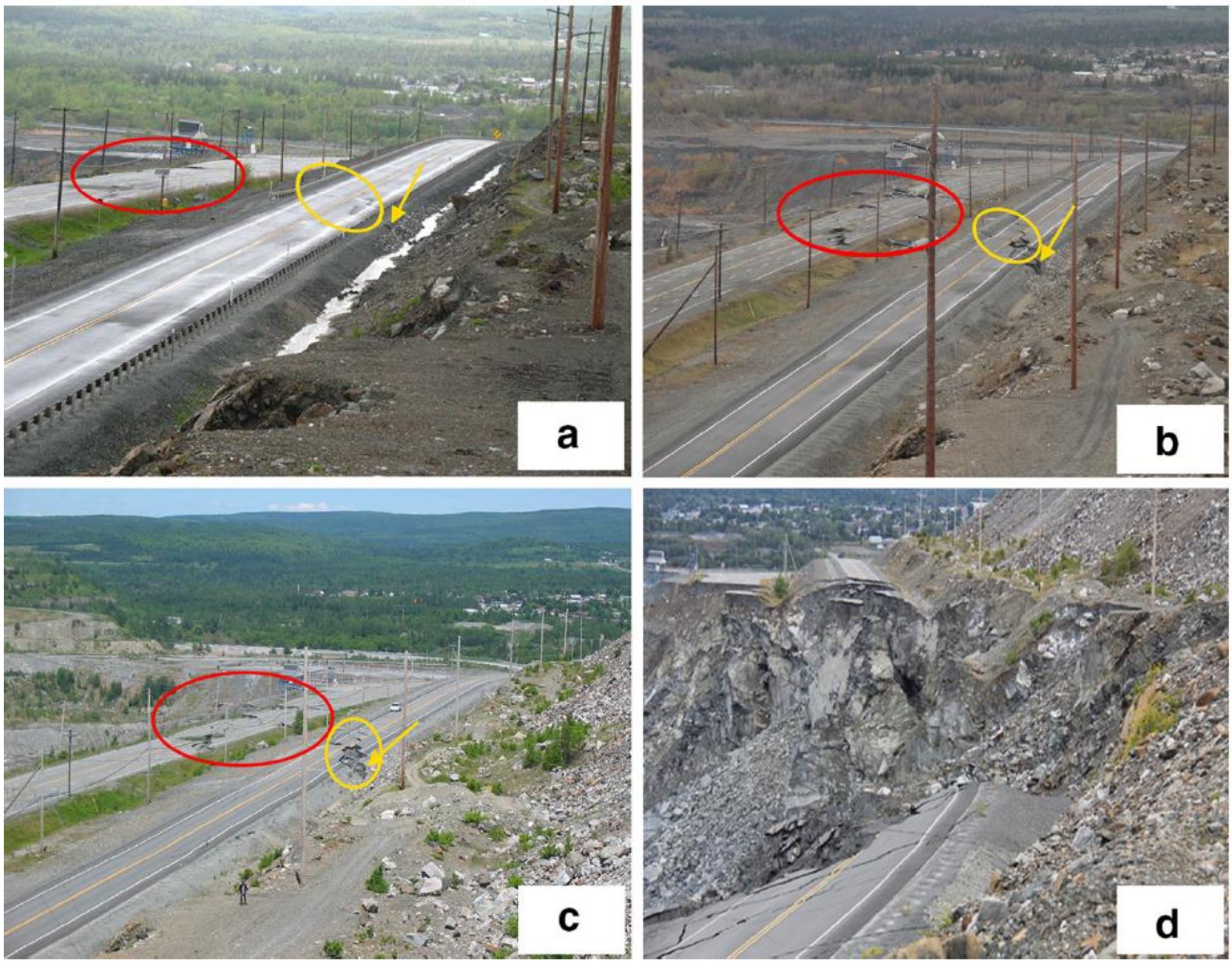

Figure 3. **a** North sector of East wall in May 27, 2011. **b** May 9, 2012. **c** June 14, 2012. **d** July 13, 2012

wide and 20 m deep. After a dry 2010 summer, no further deformations were observed that year.

In 2011, an increase in the crack extensions was observed (circled in red and yellow in Fig. 3a). In May 2011, Road 112 was closed for good. That year also marked the shutdown of the LAB Chrysotile mine. At the same time, termination of water pumping at the pit bottom was confirmed. The cracks observed on the floor of the temporary road increased in the spring of 2012 (circled in red and yellow in Fig. 3b, c); the major slide in the East wall of the main pit occurred on July 12, 2012 (Fig. 3d).

As shown on Fig. 4, the failure that occurred in the East wall, took away a large part of Road 112 over a length of approximately 800 m and a width of 100 m. The north portion and part of the south portion of the failure moved in a quasi-monolithic way over a vertical distance of 70 m, and the volume displaced was estimated to be around 25 hm^3.

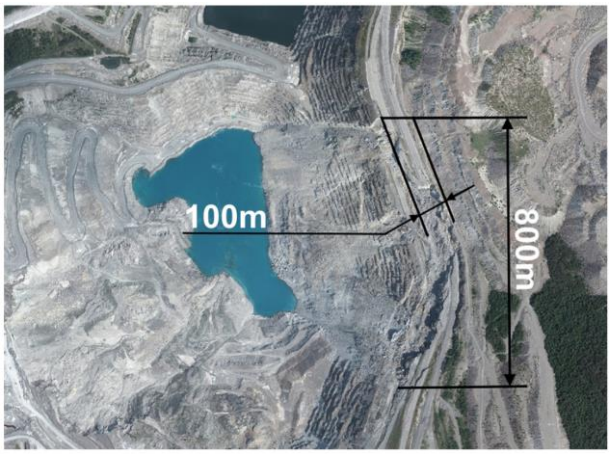

Figure 4. Airbone view of the July 12, 2012, failure

3 DATA COLLECTION, PROCESSING, AND ANALYSIS

The mine stopped surface monitoring of the East wall in 2010, and subsurface extensometer and piezometer

monitoring ceased in early 2011. Furthermore, access to the East wall was limited due to the ongoing failure. SAR methods were not deemed adequate due to the large displacements observed; such methods are limited by the wavelength of the signals, and thus only small displacements could effectively be monitored. Terrestrial photogrammetry would have required extensive site access, which was not possible at the mine site. LiDAR laser scanning (TLS and ALS) was thus selected as a way to monitor the slope failure.

3.1 Surface Survey Using LiDAR

Terrestrial and airborne LiDAR were used as the main tool to quantitatively monitor the rock slope failure on the East wall of the LAB main pit. LiDAR is a measurement tool using laser technology to scan surfaces whose area varies from square meters to square kilometers. Essentially, the two types of LiDAR used here are based on the time-of-flight technique, in which the round trip time of flight of a light pulse is measured in order to estimate the distance between the LiDAR and the object. Two measurement methods were used, one with a terrestrial LiDAR, which generates a terrestrial laser scanning (TLS) point cloud, and the other with an airborne LiDAR, which produces an airborne laser scanning (ALS) point cloud.

The advantages of the terrestrial LiDAR are easy setup, easy data acquisition using a USB key, adjustable spatial point density (which can vary from centimeters to meters), and great mobility for scanning large areas from multiple angles. Ground positioning also has the advantage of the ability to scan occlusions that cannot be reached using airborne LiDAR. However, airborne LiDAR scans larger areas of several square kilometers, doing so much faster than the terrestrial LiDAR (Abellan et al. 2014; Gordon and Charles 2008).

Scanning is limited or proscribed in the event of high humidity, rain or snow. Moreover, the number of shadow areas may be important depending on whether or not the rock surface scanning is done from a limited number of LiDAR positions and/or scan shooting angles are insufficiently large (Abellan et al. 2014; Gordon and Charles 2008). Airborne LiDAR scanning can reduce the number of shadow areas when ground positioning constraints are too high. Numerous LiDAR case studies exist, and show the technology's wide range of slope monitoring possibilities (Jaboyedoff et al. 2012; Lato et al. 2012; Ferrero et al. 2009; Froese et al. 2009; Teza et al. 2008).

3.1.1 Time Line of the Surface Survey

The LiDAR survey dates performed at the site are given in Table 1. Altogether, 18 LiDAR surveys were performed. Transport Quebec provided the ALS data for that project. They were collected four times over the span of the project between 2010 and 2014. Georeferencing of the raw data was done by a firm contracted by Transport Quebec. TLS was conducted at the site by the authors. Two surveys were performed for every TLS recording date. The distance between the LiDAR station and the East wall was within the range of apparatus range, except for the most easterly part of the wall, which was slightly beyond the optimal distance (approximately 1.8 km). The scanning range for the terrestrial LiDAR used in this study—an Ilris Optech 3D-ER (Optech 2011)—is limited to 1.8 km for a reflectivity of 80%. The raw TLS data collected by the scans between 2012 and 2014 were preprocessed using Optech's parsing software to generate organized point clouds suitable for analysis by third-party software, as done in studies conducted by other authors such as Lato et al. (2014).

Table 1. Date and type of LiDAR survey performed since the June 29, 2012, reference DTM

DTM_ID	Type of the point cloud	Fused	Year	Recording date
1	ALS		2010	November 22
2	TLS	1–2	2012	June 29
3	TLS	1–3	2012	July 11
4	ALS		2012	July 13
5	TLS	4–5	2012	August 2
6	TLS	4–6	2012	August 29
7	TLS	4–7	2012	September 27
8	TLS	4–8	2012	November 12
9	TLS	4–9	2013	June 5
10	TLS	4–10	2013	June 17
11	ALS		2013	August 5
12	TLS	11–12	2013	September 19
13	TLS	11–13	2013	October 11
14	TLS	11–14	2013	November 8
15	TLS	11–15	2014	April 8
16	TLS	11–16	2014	May 15
17	TLS	11–17	2014	July 16
18	ALS		2014	November 4

3.1.2 Survey Accuracy

One of the main interests in using ALS derives from its accurate georeferencing capability. In this case, the horizontal coordinates x and y are georeferenced relative to the coordinate system associated with the projection system NAD83 CSRS MTM 7. For the vertical coordinate system (the height—z), the NGVD 1929 is used. According to the firm contracted by Transport Quebec, the absolute accuracy range of ALS is ±15 to 25 cm in altimetry and ±15 to 25 cm in planimetry. The LiDAR system used in 2013 was the Riegl Q680i, and it was the Optech Gemini in 2014. For an Ilris Optech 3D-ER, used to perform the TLS, the manufacturing accuracy of the raw data at 1 sigma is 7 mm at a distance of 100 m.

3.1.3 Methodology Used to Combine and Align ALS and TLS

The most recent ALS were used to align the TLS using discrete points and best-fit alignment procedures such as the one presented by Lato et al. (2014). Altogether, 14 fused (combined) ALS–TLS were generated (see Table 1). ALS–TLS 1–2 is defined as the baseline. Since the failure occurred on July 12, 2012, and TLS monitoring began in

June 2012, and the geometry of the pit was captured before and after the major failure.

Figure 5 shows the approach used in this work to create a digital terrain model (DTM) with one ALS and two TLS. In the example shown, two TLS are recorded from different positions in the main pit at a given date, according to the guidelines provided by Bonnaffe et al. (2007). The TLS recordings only target the east area of the open pit. In Fig. 5 the two point clouds belonging to the TLS are visible in yellow and green. The point cloud associated with the ALS is shown in the background in gray. The records from two different LiDAR positions allow covering a large area of the East wall.

The final step consists of aligning the merged TLS with the ALS. To do so, points on both the ALS and the TLS that did not experience displacement are selected to perform the alignment. In the case presented, the granite dyke between the two pits—which is considered to show no displacement during the monitoring period—is used as the support for the alignment. This was achieved using a combination of visually recognizable ground features and mathematical iterative best-fit algorithms as described by Lato et al. (2014). Finally, in the area that experienced displacements, the ALS data were removed, in order to keep only the TLS data. The final result is a single georeferenced point cloud on which the meshing can be performed to produce a DTM.

3.1.4 Change of Detection Threshold

As proposed by Lato et al. (2014), the limits of ‘‘actual change’’ versus alignment error or signal noise can be determined through analysis of portions of the dataset where minimal change had occurred. A region of minimal change, located in the granite dyke, was mapped in all surveys. This was achieved using an iterative analysis of change detection calculations in combination with a visual examination of the terrain. Figure 5 shows the selected zone (numbered 1) on the rock slope, comprising an area of 4486 m^2. The distribution presented on the histogram shows the mapped change (in meters) between two point clouds within this zone and the fitted normal distribution for a typical analysis performed.

Table 2 presents in detail a comparative quantitative analysis for this region of minimal change during the entire investigated period, for the sequential fused ALS–TLS using the fused ALS–TLS (1–2) as the baseline and using the point to mesh tool in CloudCompare (2016). The number of observations range from almost 400,000 points in the first surveys to 12,000 in the final ones. The declining number of observations is explained by the limited access

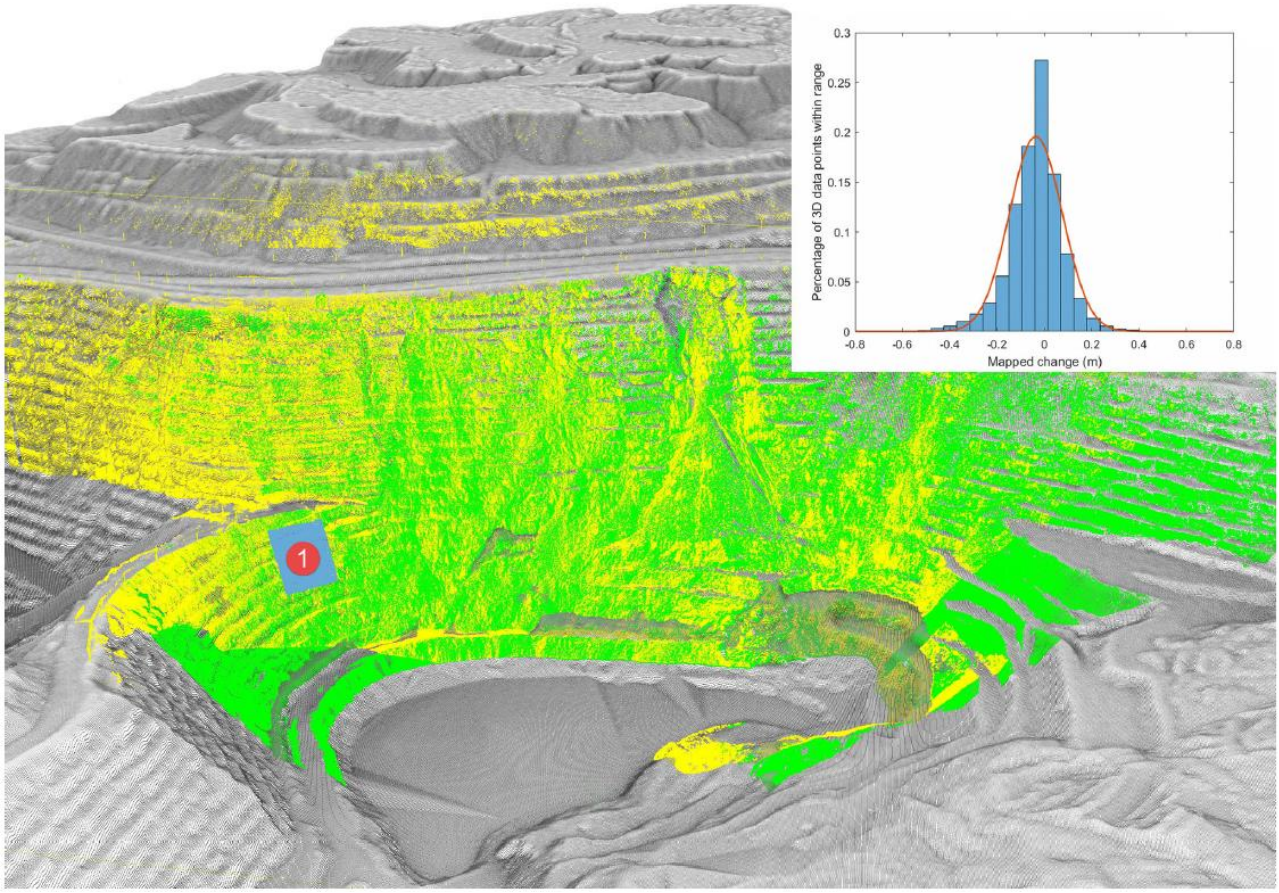

Figure 5. Creation of a DTM with a combination of two TLS and an ALS. Identification of a zone with minimal change (1). Histogram of mapped change between two point clouds in this zone (color figure online)

Table 2. Dataset selected to evaluate change detection threshold

Fused ALS–TLS	Observations	Mean (m)	Std (m)	Median (m)	Passing 2.3%	Passing 97.7%	KS test	Skewness	Kurtosis
1–3	334,370	−0.0359	0.1121	−0.0250	−0.3050	0.1810	1.0000	−0.4170	5.0007
4–5	338,116	−0.0090	0.0602	−0.0150	−0.1100	0.1350	1.0000	0.7539	4.3427
4–6	371,566	−0.0208	0.0516	−0.0230	−0.1150	0.0960	1.0000	0.4941	4.3978
4–7	382,056	−0.0352	0.0647	−0.0370	−0.1560	0.0970	1.0000	0.2072	3.1399
4–8	201,112	−0.2842	0.7301	−0.2860	−1.6470	1.2680	1.0000	0.2540	3.1423
4–9	143,859	−0.0237	0.1405	−0.0350	−0.2930	0.2770	1.0000	0.2410	3.0015
4–10	117,678	−0.0946	0.2536	−0.0690	−0.7080	0.3470	1.0000	−0.5411	4.1624
11–12	20,602	−0.0343	0.1266	−0.0650	−0.2070	0.2810	1.0000	1.0496	4.4762
11–13	75,902	−0.0612	0.1423	−0.0930	−0.2730	0.2770	1.0000	0.8027	3.3506
11–14	44,896	−0.0647	0.1663	−0.1050	−0.3050	0.3100	1.0000	0.8022	3.4278
11–15	12,263	−0.0192	0.1452	−0.0620	−0.1990	0.3270	1.0000	0.9090	3.6103
11–16	15,227	0.0605	0.2853	0.0260	−0.4600	0.7400	1.0000	1.2527	7.9833
11–17	12,286	−0.0190	0.1451	−0.0610	−0.1990	0.3260	1.0000	0.9054	3.6003

Successive surveys are compared with the fused dataset (ALS 1 and TLS 2)

to the initial survey stations over time due to the pit infilling with water after pumping ceased.

A Kolmogorov–Smirnov (KS) test was used to test the null hypothesis that the data—the mapped change in meters-comes from a standard normal distribution against the alternative that it does not come from such a distribution. The test rejects the null hypothesis at the 5% significance for all datasets. Kurtosis, a measure of how outlier-prone a distribution may be, was also evaluated. The kurtosis of the normal distribution is 3. Distributions obtained for the sequential fused ALS–TLS are slightly more outlier-prone than a normal distribution. Skewness, a measure of the asymmetry of the data around the sample mean, was evaluated. If skewness is negative, the data are spread out more to the left of the mean than to the right. The skewness of the obtained distributions are slightly different from zero, which would be typical of any perfectly symmetric distribution such as the normal distribution. As mentioned by Abella´n et al. (2011) and others, when an actual change is not adequately defined by a normal distribution, the standard deviation cannot be used to define error, and the percentile of the error should alternatively be used. In Table 2, the 2.3 and 97.7% percentiles are presented for all fused sets. For the vast majority of the fused sets, these percentiles range between ±0.30 m, with some larger values up to ±0.75 m for two sets. Fused dataset 4–8 was rejected due to an abnormally large error partially linked to a thin layer of snow present on the ground. The error could thus be very conservatively assumed to be within ±1 m. As mentioned by Lato et al. (2014) and Abellan et al. (2011), within these limits the difference between error and change cannot be confidently determined. It is important to mention that this threshold is less than 1% of the maximum displacements investigated.

3.2 Data Analysis

Sequential fused ALS–TLS can be used to characterize terrain geometry and to monitor changes in the slope. The next sections will describe briefly the approaches used in this project in the context of very large (hectometric) rock mass displacement.

3.2.1 Terrain Geometry

Fused ALS–TLS can be used to characterize the geometry of the rock slope and give a precise state of the geometry at a given point. It can provide information on the geometry of the slope, the volume extracted during the mining work and also on the pit volume. Fused ALS–TLS can also be used to capture the altimetry of a water surface. In the present case study, pumping in the pit had stopped and the water level in the pit was rising. As it was shown in Grenon et al. (2016) the water level in the pit was critical in controlling slope stability. The water level at the bottom of the pit is modelled with a plane. Water is considered as a shadow area in TLS. Consequently, the foot of the rock slope obtained for a given TLS is considered to be the water level at that date and time. ALS scans enable interpreting these specific shadow zones as a water source and representing them as a planar point's surface.

3.2.2 Differential Volume Measurements

Differential volumes can be established by comparing a base case DTM with a second DTM, and then computing the volume difference between the two DTMs. Differential volumes are considered to be positive or negative. Figure 6 schematically presents the concept of negative and positive differential volumes in 2D. At the crest of the slope, a negative volume can be computed to define slope instability. At the toe of the slope, a positive volume can be computed for the same purpose. The usefulness of differential volume measurement between two DTMs has already been demonstrated in many case studies, such as those presented in Abella´n et al. (2009, 2010), Froese et al. (2009), Eberhardt et al. (2007), Corsini et al. (2007) and Squarzoni et al. (2003). Monitoring the positive and/or the negative volumes leads to accurate monitoring of the displaced volumes. However, this method generates no quantification of the displacements. In this case, since the

water level is rising and thus hiding the base of the slope, only the negative volume was used.

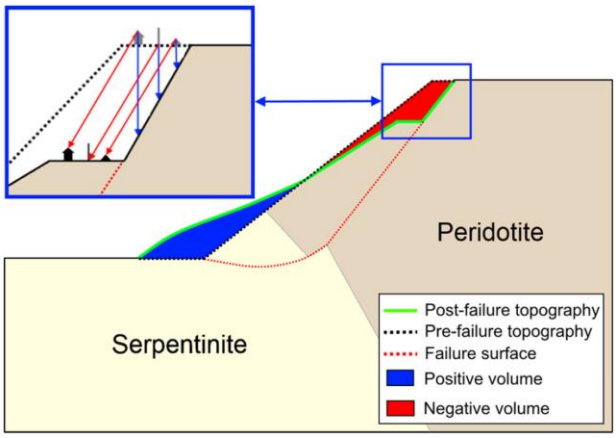

Figure 6. Computing positive and negative differential volumes, differential elevation (blue arrows in the enlarged area) and total displacement (red arrows in the enlarged area) (color figure online)

3.2.3 Differential Elevation Measurement

Differential elevation can be computed by subtracting the elevation values obtained at a single (x, y) location on two DTMs. This operation is routinely carried out using software tools, such as ArcMap (ArcGIS 2010) or PolyWorks (InnovMetric Software Inc. 2012). It can be performed on point clouds or on rasterized data. The principles of this concept are shown in Fig. 6. The differential elevation measurement is represented by blue arrows. This technique has proven effective in terms of surface monitoring for some rock surfaces. Prokop and Panholzer (2009) showed how this technique enabled them to detect and locate erosion areas and embankments on a large rock surface. The principal weakness of this technique is that it considers only vertical variations. If the horizontal displacement component is important in the investigated case study, the results obtained should be interpreted carefully.

3.2.4 Displacement Vector

An alternative approach would be to compute the magnitude of the total displacement that occurred between two DTMs. This approach would give a more complete representation of the slope movement. The principles of this concept are shown in Fig. 6. Total displacement is represented by red arrows. In this example, the location of the roof of a surveyor cabin, the foot of an electric pylon and the top of rock berm are points that can be easily followed during slope failure. Their location before the failure (colored in gray) and after the failure (colored in black) are shown in Fig. 6. In this specific example, evaluating the total displacement magnitude provides a more effective way of capturing rock mass movement than differential elevation quantification. A limitation of this latter approach is that reference points are necessary to match the two DTMs. These points are not always easily identifiable in the field.

Total distance measurements could be computed using standard total station measurements and reflecting prisms in the field. The limitation of such an approach is that the monitoring is limited to the targeted points. Combining DTM with prism information provides a means to extrapolate the displacement results to the entire slope surface. Without monitoring prisms, the DTM approach can still be effective using recognizable points on the slope surface (surveyor cabin, electric pylon, bench crest, railing and any other geometric elements displaying singularities) can serve as reference and anchor points. Thus, it is possible to compute total displacements, and consequently quantify the displacement magnitude. One must be careful however, as this technique only works if intact areas of the rock mass are preserved during the failure in order to identify them during the monitoring period.

Computing total displacement further enables establishing displacement orientation. In other words, the displacement vector obtained allows computing the magnitude and orientation of the total displacement. For slow moving failures, algorithms exist in the literature for automatically computing these displacement vectors, as in Fruneau et al. (1996), Teza et al. (2007, 2008), Monserrat and Crosetto (2008), Oppikofer et al. (2008), Travelletti et al. (2008), Pesci et al. (2011), Carrea et al. (2012). These techniques have smaller errors than shortest distance comparisons and can be used for the detection of small displacements (centimetric level) in rock slopes. The advantage of such an approach is its ability to detect and accurately quantify the movement and define the acceleration of an unstable area. For large displacements, such as the one involved in the case study, the displacements are hectometric in scale, and to the author's knowledge, it is not yet possible to automate the process. Singularities in the DTMs must be visually identified. When more singularities are used, the best estimation of the global displacement vector can be achieved. For different zones of a rock face, mean displacement vectors can be assessed for various time periods.

4 FIELD MONITORING RESULTS

The results of the various comparisons between fused ALS–TLS and the baseline are given in the next sections. Results are presented for terrain geometry assessment, differential volume, differential elevation, and total displacement assessments.

4.1 Terrain Geometry Assessment

The DTM produced based on the survey available from TLS could thus be combined with the most recent ALS available at the time to produce a global DTM for every recording date (Fig. 7). Figure 7 enables following the evolution of the slide and the raise in water in the pit. Table 3 presents some of the most important geometrical characteristics of the investigated rock slope. The slope height is 335 m, and the overall slope angle is 40° on average. The altitude (height above mean sea level) of the

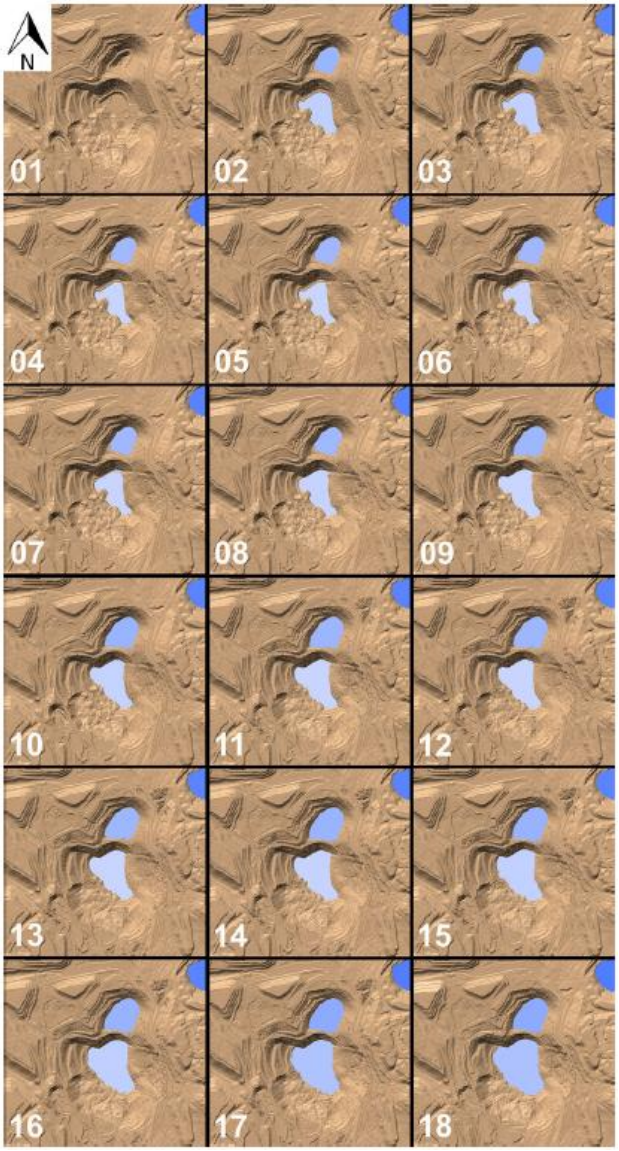

Figure 7. LAB Chrysotile mine DTMs from June 29, 2012, to November 4, 2014

Table 3. Parameters of the east wall from the DTM on July 11, 2012

Parameters	Data
Road 112	Altitude = 299 m, width = 90 m
Depth of the pit	Altitude = −36 m
Berm geometry	Height = 12.2 m, width = 6.1 m
Overall East slope	Height = 335 m, global angle = 40°
Water in pit	Initial water elevation −14.7 m

water level at the bottom of the pit was measured as -14.7 m from the DTM obtained on July 11, 2012, the day before the failure of the East wall. The blue curve in Fig. 8 shows the water surface elevation evolution for the monitoring period. The black curve in Fig. 8 represents the volume of water accumulated in the pit, obtained using both pit volume and water surface elevation. According to the mine restoration plan, the elevation of the lake outlet will be 233 m. This outlet will be created anthropically, and the outlet will reach a river nearby. Assuming that the water table line is at 233 m, the pit should thus be filled by 2035.

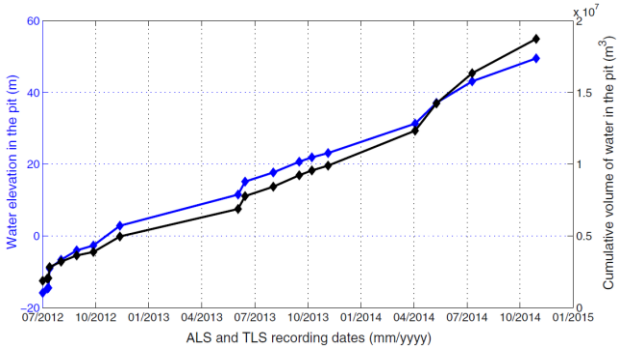

Figure 8. Water surface elevation in the pit obtained with LiDAR survey (*blue line*) and cumulative volume of water in the pit (*black line*)

4.2 Differential Volume Analysis

The first means of quantification used for the sliding on the East wall of LAB Chrysotile mine, is the 3D differential volume quantification. The focus is on the negative volume evolution at the crest of the slope. Figure 9 presents the cumulative negative volume generated in this area. The points on the curve show the results for the cumulative differential volume quantification starting with the DTM recorded on June 29, 2012, and the following DTMs.

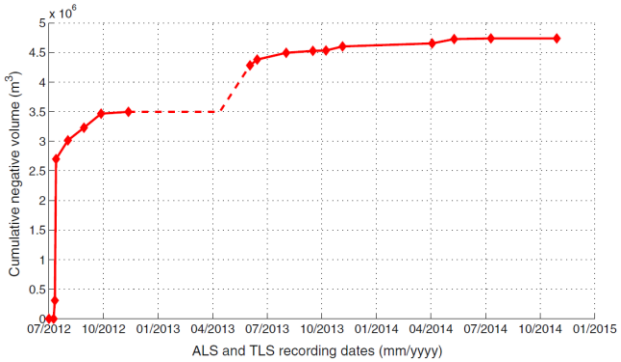

Figure 9. Evolution of the cumulative negative volume during the monitoring period

Between July 9 and July 11, the sudden increase in the volume was a precursor to the failure that occurred on July 12. The ALS recorded on July 13, 2012, shows that the negative volume suddenly increases from 0.3 hm^3 on July 11 to approximately 2.7 hm3 on July 13. The failure continued to be active until its stabilization after November 12, 2012, with a negative volume measured at 3.5 hm3. As no measurement was performed during the 2012–2013 winter and spring periods (dashed line in Fig. 9), the authors reasonably assumed that during the freeze-up period (December 1, 2012, to April 15, 2013), the displacements were negligible, corresponding to a marginal change in differential negative volume. The first

TLS recorded in 2013 was on June 5. The cumulative negative volume increased to 4.3 hm3. The curve seems to taper off after this point, and stabilized at the beginning of the 2013 winter. Few changes were observed during 2014, and the slight increase in negative volume can be explained by washout on the escarpment zone. The curve in Fig. 9 shows that the sliding follows an ‘‘active-stable’’ cycle for the first 2 years of monitoring, likely associated with seasonal temperature changes in the region. This cycle was not observed in the Winter of 2014.

4.3 Differential Elevation Analysis

This section presents the differential elevation analysis for the East wall. This analysis was performed using PolyWorks (InnovMetric Software Inc. 2012). Two maps were produced. The first map was obtained comparing the prefailure DTM obtained on November 22, 2010, and the post-failure DTM obtained in August 5, 2013 (2013 map, Fig. 10). The second map was obtained comparing the November 22, 2010, and the November 4, 2014, DTMs (2014 map, Fig. 10). The limit of detectable change was conservatively fixed at 1 m based on the analysis presented in Sect. 3.

The white line drawn on the Fig. 10 maps defines the extent of the unstable area where large displacements were visually observed in the field. The blue line on the same map defines the extent of the unstable area as quantified using DTM differential elevation analysis. This map thus allows quantifying the limits of the slide and the magnitude of the differential elevations over the entire failure surface. The external limit (blue border) is confirmed in the field by the presence of tension cracks.

Differential elevation measurements presented in Fig. 10 (2013 map), and Fig. 10 (2014 map) are color coded based on the magnitude of the differential elevation. In both cases, the maximum value is close to 80 m and is located in the northern area of the failure. It also shows a much smaller differential elevation in the southern part of the failure. This difference between the north and south areas suggests heterogeneous movements when the failure occurred. Furthermore, it shows that the differential elevation quantification in the upper part of the northeast portion of the failure zone is much more important than the differential evaluation quantification in the lower part of northeast portion of the failure zone.

Comparing the northern area of the Eastwall in Fig. 10 (2013 map) and Fig. 10 (2014 map), shows that washout of the escarpment associated with localized rock falls can explain most of the differences between these two maps. The southern area, although less affected, shows differential elevation quantification of around 5 m, which slightly increased between 2013 and 2014 (Fig. 10, 2014map). Indeed, focusing on the south portion of the unstable zone, the failure extent remained almost the same between 2013 and 2014 (250 m), while the magnitude of the differential elevation in this area slightly increased. Looking more closely at this area, situated between the

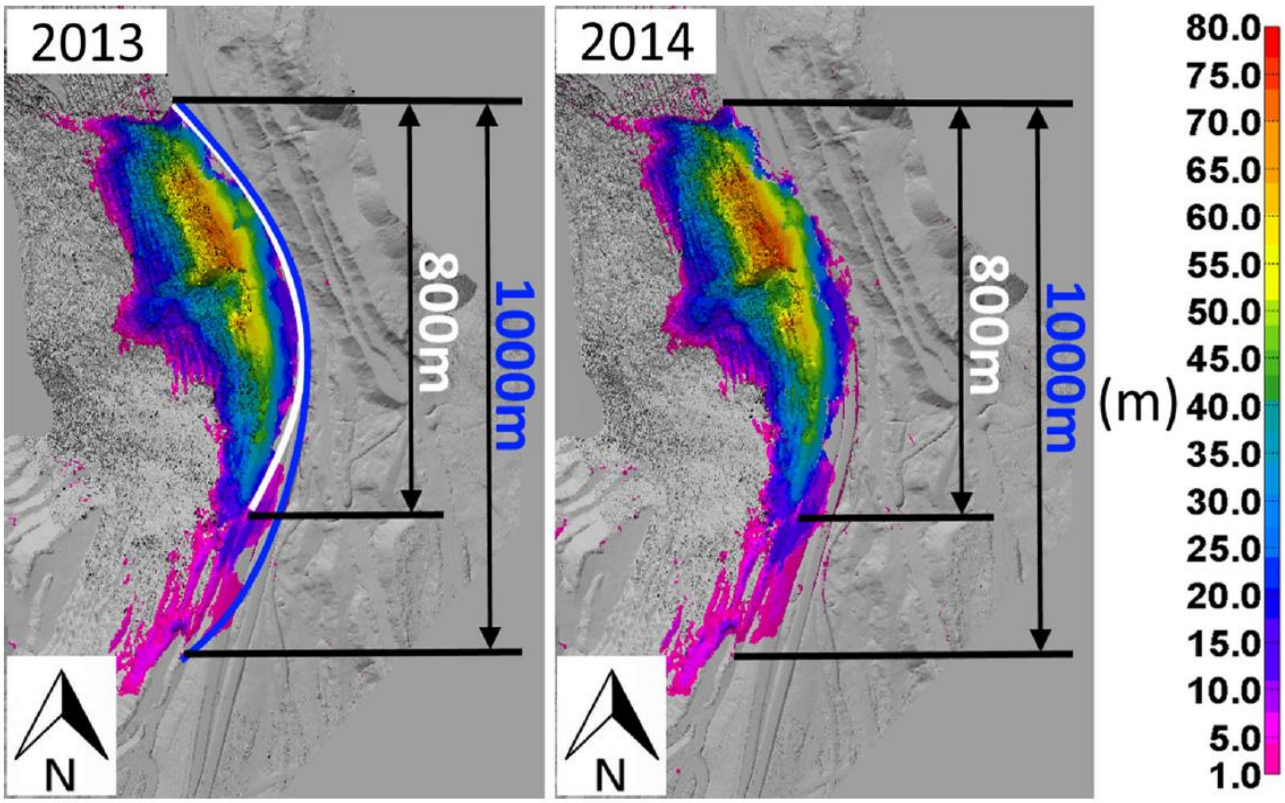

Figure 10. Quantification of the differential elevation (m) between the DTM recorded on November 22, 2010, and on August 5, 2013 (2012 map), and between the DTM recorded on November 22, 2010, and on November 4, 2014 (2014 map)

borders defined by the white and blue lines, the magenta color has slightly intensified, and the coverage of this area is more continuous in the 2014 map than in the 2013 map in Fig. 10.

4.4 Total Displacement Evaluation

This section presents the results of a vector analysis of the total displacement that occurred on the East wall. It will enable reporting on the extent of the failure zone and then analyzing the evolution of total displacement over that 3-year monitoring period for various regions of the pit. It will further enable a better understanding of the kinematics of the sliding.

4.4.1 Division of the East and Southeast Walls into Sectors

Field observations and differential elevation analysis have suggested that the failure movements are heterogeneous. To take into account these observations, the East and Southeast walls are divided into six distinct sectors (Fig. 11). Road 112 is associated with Sector 1, the upper part of the North Zone of the East wall with Sector 2, the upper part of the eastern part of the East wall with Sector 3, and the lower part with Sector 4. For the sectors in the Southeast wall, the upper part is associated with Sector 5 and the lower part with Sector 6.

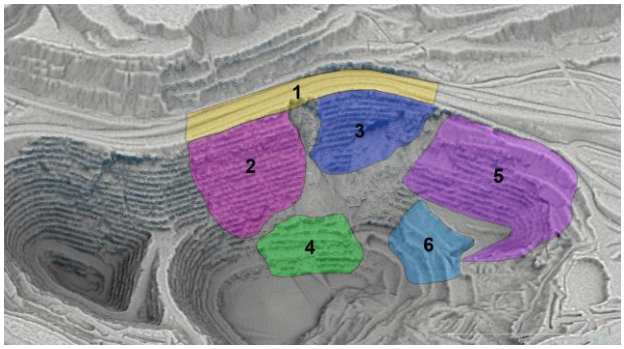

Figure 11. Division of east and southeast wall into six sectors

For a better understanding of the segmentation of the East and Southeast walls, the average orientation of the overall slope for each of these walls is given in Table 4. These average orientations for the East and Southeast walls are measured from the base case referential DTM recorded on June 29, 2012. For the East wall, the average measurement result (dip and dip direction convention) is 42°/250°. For the Southeast wall, slope orientation is computed from the same DTM by considering separately the upper part (sector 5) and the lower part (sector 6) of the slope. The lower part of this wall was put in place as an abutment. The slope orientation for the upper part of the Southeast wall (Sector 5) is 36°/295° and for the lower part of the Southeast wall (Sector 6) it is 31°/320°.

Table 4. Mean slope orientation for the various sectors measured from the June 29, 2012 DTM

Wall ID	Sector ID	Average orientation	
		Dip	Dip direction
East	2, 3 and 4	42°	250°
Southeast	5	36°	295°
	6	31°	320°

4.4.2 Total Displacement Orientations

Qualitative field observations clearly indicate that there is a strong evidence of a horizontal component in the sliding orientation. The objective of this section is to quantify the orientation for the total displacement associated with each of these six sectors whose limits were defined in Fig. 11.

Displacement orientation results for all sectors are presented in Table 5. For every sector, the number of points used to derive total displacement orientation is showed. Sectors 1 and 6 are characterized by a smaller number of points. The resulting mean total displacement is presented in two ways: the first uses a mean trend and plunge, and the second one presents their mean Cartesian components. For Sectors 1–4, it appears that the trend is similar. The plunge is higher in the upper part of the failure, at 55° in Sector 1, reduced to 45° in Sectors 2 and 3. The total displacement is almost horizontal for Sector 4, with a plunge of 6°.

For Sectors 5 and 6 the same observations apply. The orientation trend is similar while the plunge differs. Again the sector at the bottom of the pit shows an almost horizontal displacement. Sector 5 shows a flatter displacement orientation than what was observed on Sectors 2 and 3 located at a similar height, suggesting a clearly different mass movement on that side of the slide.

The Fisher constant obtained for Sectors 1–4 suggest moderate variability within the vectors used to define mean

Table 5. Total displacement orientation quantification by sector during the survey period

Sector ID	No. of survey points	No. of displacement vectors	Trend/plunge	Unitary displacement vector (cartesian components)			*K* (Fisher)
				East	North	Elevation	
1	13	65	275°/55°	−0.57	0.05	−0.82	26
2	11	176	270°/45°	−0.71	0.00	−0.71	23
3	12	147	280°/45°	−0.70	0.12	−0.71	21
4	13	147	260°/06°	−0.98	−0.17	−0.11	28
5	55	135	292°/20°	−0.87	0.35	−0.34	17
6	10	24	314°/03°	−0.72	0.70	−0.05	91

orientation. The dispersion is similar for all four sectors. On the contrary, in Sector 5 the vectors are extremely spread out, thus less confidence is associated with the determination of the mean value. Sector 6 suggests that all vectors are strongly similar in orientation.

4.4.3 Total Displacement Magnitude

The total displacement magnitudes were computed between successive DTMs. These magnitudes were computed based on the vectors introduced in Table 5. Figure 12 presents the total cumulative displacements for the surveyed points for Sectors 1–4 recorded at every LiDAR scan date. The various sectors present some differences in the results. Sector 1 has the largest displacements while Sector 3 features the smallest displacements.

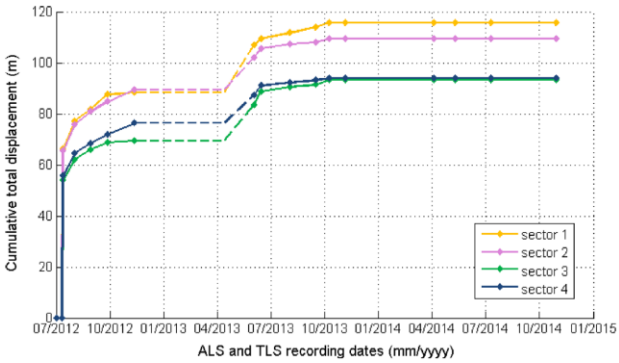

Figure 12. Magnitude of the cumulative displacements along the direction of the average displacement vector for Sectors 1, 2, 3 and 4

For another look at the computed displacement results, the monitoring period is divided into four periods (Table 6). The first period covers the time around the major failure that occurred on July 12, 2012. The second covers the year 2012 after the July 12 failure. The third covers 2013, and the fourth the year 2014 (note that the dates listed in Table 6 refer to the LiDAR recording dates). For each sector of the East wall, the magnitude is measured consecutively between each period along the survey points. It is important to note that during the Winter and Spring of 2012–2013, no LiDAR survey was performed. This is shown by dashed lines in Fig. 12.

During the first period, the magnitudes in Sectors 1 and 2 are identical and 10 m higher than the magnitude in Sector 3. The displacement magnitudes of these sectors show some small differences during the sampling period. The Sector 3 displacements are lower than those in Sector 2 during the second period, and become larger during 2013 (period 3).

The displacements in Sector 4 are measured on the surface above the pit water level at the scan date. This surface decreases as the water level in the pit rises. Furthermore, the coverage of the entire zone with survey points is not possible because of the rising water.

Finally, the differential displacements measured for Sectors 1, 2, 3 and 4 between 2013 and 2014 are null. This result shows that the slide did not progress significantly during this period. It is important to mention that even if the magnitudes of cumulative displacements vary between the sectors, all sectors experience large total displacements (between 90 and 115 m). Large displacements are thus observed and quantified at the top and at the bottom of the slope.

The monitoring of the South wall was not as accurate as on the East wall, because of the large distances between TLS and the wall. Consequently, only the DTMs made with ALS were used to measure the differential displacements. The DTM used as a reference point for the measurements was derived combining the DTM recorded on November 22, 2010, and that recorded June 29, 2012. Displacement in this area occurring before the latter date was thus not quantified.

Total displacement was measured along the survey points and is presented in Table 5. It shows that the movements are constant at 5 m for the 2 first periods in Sector 5. It is important to note that it is not possible to know whether the displacements occurred mainly at the end of 2013 (between August and December) or are evenly distributed between the two DTM dates (August 5, 2013, and November 4, 2014). Regarding the third time period, the displacements halved for Sector 5. In Sector 6, the movement is 2.5 m in the first period and around 1 m for the next two periods. The latter results are at the fringe of the detection change threshold.

4.4.4 Maps of Total Displacements

This section presents the creation of total displacement magnitude maps for the entire pit area on a sector-by-sector basis. Total displacements are computed based on the mean total displacement vector associated with a sector for the surveyed points presented in Table 5. The heterogeneity of the displacement values is observable and, most importantly, spatialized on the maps. The limit of detectable change was again conservatively fixed at 1 m based on the analysis presented in Sect. 3.

Table 6. Magnitude of total displacement for the monitoring period

Sector ID	Magnitude of total displacement (m)			
	From November 22, 2010, to July 13, 2012	From July 13, 2012, to November 12, 2012	From November 12, 2012, to November 8, 2013	From November 8, 2013, to November 4, 2014
1	66	22	27	0
2	65	24	20	0
3	54	16	24	0
4	56	21	18	0

These maps have the advantage of providing a visualization of the total displacements over the entire DTM recorded between June 29, 2012 and the subsequent dates, as well as of the evolution of the failure during the monitoring period. These maps quantify the evolution of the actual displacements in the targeted sectors. The maps of cumulative displacement magnitudes (along the average displacement vector orientation for those sectors) are shown for Sectors 1, 2, and 4 in Fig. 13.

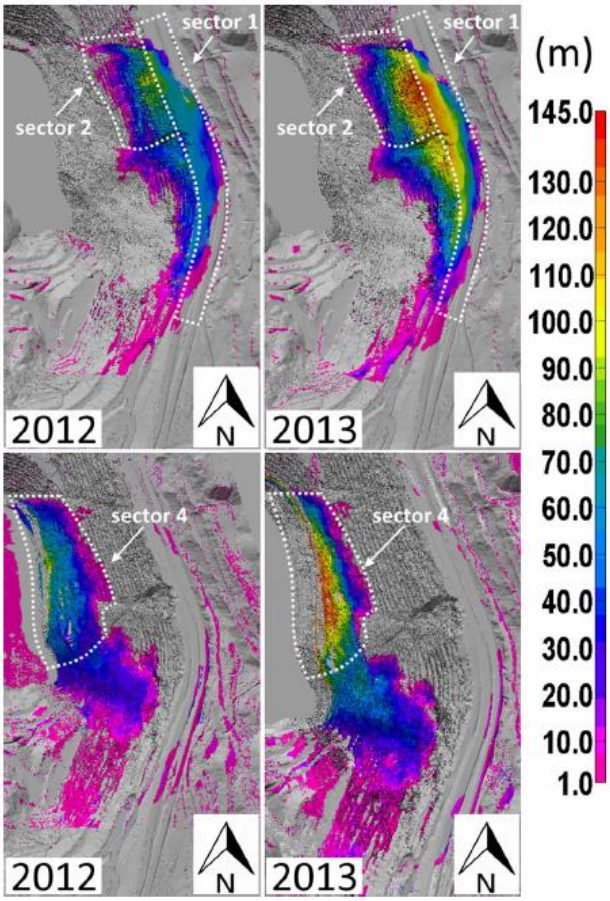

Figure 13. Magnitude of cumulative total displacements in Sectors 1, 2 and 4 during the following two periods: November 22, 2010–July 13, 2012 (2012 map); November 22, 2010–August 5, 2013 (2013 map)

Looking at Sectors 1 and 2, it can be observed that the maximal total displacement is between 130 and 145 m. This value is slightly higher than the one showed in Fig. 12 for this same sector. This could be explained by the fact that the survey points in Sector 1 did not cover this exact area of maximum magnitude. In fact, the survey points were recorded in the area just to the south of this maximal displacement zone, and that area is characterized by displacements of about 115 m and 120 m, as it was expected from Fig. 12. The maps thus provide a more complete picture of the actual displacement on the 3D surface. What can also be observed is that in Sector 1 the displacements decrease as we move toward the south of the pit. This agrees with field observations and with what is now quantified in 3D space.

Looking at Sector 4 in Fig. 13, one can see that the total displacement magnitude in the lower part of the northeast portion of the failure is comparable to that observed in the upper part of the slope. The same discrepancies between Figs. 12 and 13 for this sector can arguably be explained by the localization of the survey points. It is thus reasonable to say that total displacements in Sectors 2 and 4 are comparable in magnitude and in trend but that their plunges are totally different, as stated in Table 5. This type of quantitative information is invaluable in defining the geometry (shape) of the failure surface and the failure kinematic.

Concerning the upper part of the Southeast wall (Sector 5), the map of differential displacements between DTM (Fig. 14) is computed based on the average vector for the total displacement measured at 292°/20° (Table 5). For each map, the few color variations can be interpreted as a homogeneous distribution of displacement. The upper part of the Southeast wall slides globally homogenously. Otherwise, the color tends to change between each date. The 2012 map is characterized predominantly by the color magenta, indicating displacements of 1.5–3 m. The 2013 map is predominantly defined by the color purple, indicating that the total displacements are between 3 and 7 m.

4.5 Summary and Discussion of the Different Approaches

LiDAR laser scanning of a rock slope was shown in this paper to be a very powerful way to quantitatively monitor the surface of a very large rock failure with hectometerscale displacements, even in the absence of any other quantitative monitoring of the slope. The first type of analysis showed how LiDAR results can provide geometrical information on the entire pit area and on the rise in the water level at the bottom of the infilling pit. The second type of analysis focused on differential volume assessment. This analysis provided information on the sliding volume. It also provided quantitative information on the slope movement cycles and the slope's apparent stabilization since 2014. The third type of analysis focused on differential elevation assessment. This analysis enables a quantitative assessment of the spatial variability in the rock slide movement. It also suggests that the vertical component of the slide is important in the upper part of the slope. The fourth type of analysis focused on total displacement vector assessment. It allowed quantifying both the failure orientation and magnitude. The technique presented shows how displacements can be accurately followed during a long survey period. It did highlight the fact that the magnitude of the slide was much more important in the north portion of the failure zone than in its southern portion. It then also enabled calculating that in the east–west direction the displacements were of the same order of magnitude for the entire north part of the slide. For example, the displacement magnitudes in Sectors 2 and 4 were comparable. The previous means of quantification presented in this paper did not allow such a measurement. One can also note that the total displacement magnitudes

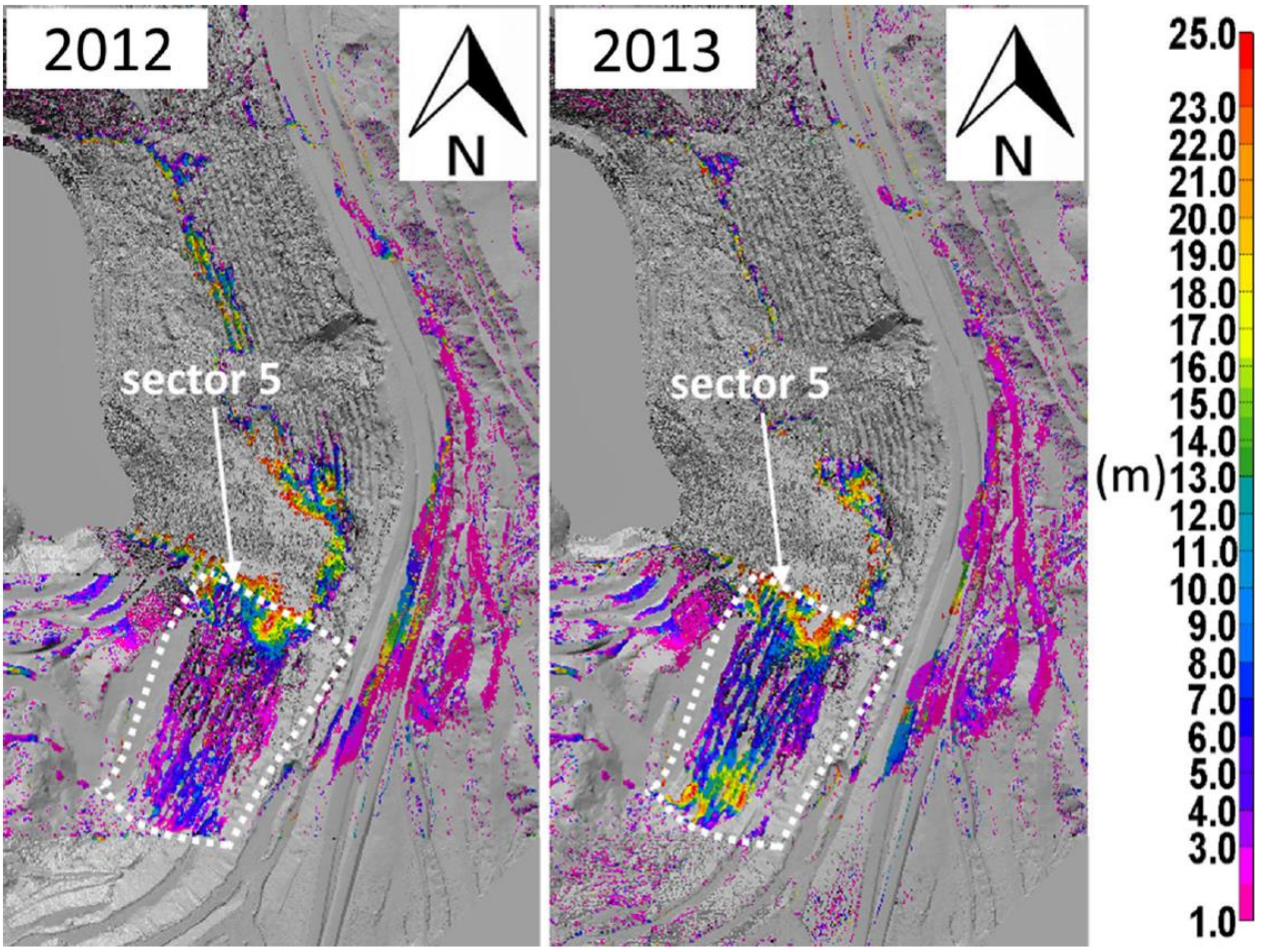

Figure 14. Magnitude of cumulative displacements in Sector 5, during the following two periods: November 22, 2010–July 13, 2012 (2012 map); November 22, 2010–August 5, 2013 (2013 map)

are much larger than the differential elevations that are computed and presented. This clearly indicates that the rock mass movement has a strong horizontal component and that displacement orientation should be investigated. Maps of total displacements give a particularly realistic representation of the tridimensional nature of the failure. Subdividing the slope studied into sectors is advisable in order to represent adequately the 3D nature of the total displacement. This approach also enabled computing the sliding direction. It shows clearly that the upper part of the East wall was sliding at a plunge of 45°-55° while the bottom part was more or less horizontal. Differential elevation analyses were not able to fully capture this behavior. The results obtained arguably suggest that the failure type is quasi-circular in shape. Furthermore, the geometry on the failure surface at the crest of the slope was captured with LiDAR scanning. LiDAR scanning can thus provide invaluable information for calibrating the back analysis of a slope failure using numerical modelling, as this can considerably reduce the geometrical uncertainty associated with the back analysis modelling process. The accompanying paper, Grenon et al. (2016), will make use of the LiDAR analysis results presented in this paper to better understand the driving mechanisms behind the East wall failure using numerical modelling.

Whereas LiDAR-based total displacement analysis is a powerful monitoring tool, some specific conditions must be present to enable such an analysis for hectometer-scale displacement monitoring as in the case under study. In fact, this technique is applicable where the mass in movement is relatively intact over the course of the survey period. Moreover, the survey surface should present asperities in order for some recognizable points to stand out. In this case, it was possible to visibly detect different geometric singularities during the survey period. These singularities can be used as anchor points for the vectors and to allow monitoring the displacements. There should be a sufficient number of them to cover the entire area of interest.

5 CONCLUSIONS

A major mining slope failure occurred in July 2012 on the East wall of the LAB Chrysotile mine in Canada. The major consequence of this failure was the loss of the local highway (Road 112), the main economic link between the region and the Northeast USA.

This case study is of particular interest for several reasons: a very large displacement occurred and the failure was active for a long period of time; mining work and the rise of the water level in the pit played an important role in the magnitude and timing of the slope failure because the pit was not in operation at the time of failure, and no conventional monitoring devices were functioning or could be installed because of the difficult site access. For all those reasons, LiDAR monitoring could provide invaluable quantitative information to help our understanding of the failure mechanism involved. The accompanying paper Grenon et al. (2016) presents a back analysis of the slope failure based on the LiDAR analysis results obtained.

This paper presented the LiDAR monitoring of this slope failure. The main focus was the investigation of that rock slide using both TLS and ALS. Since 2010, four ALS and fourteen TLS were performed to characterize and monitor the slide. Laser scanning was first used to investigate the geometry of the slide. It was then used to investigate the rock slide 3D displacement, thus enabling a better understanding of the sliding kinematics. This paper clearly shows the ability of LiDAR scanning to provide valuable quantitative information on large rock mass sliding. Furthermore, it underscores the advantages of using a vector quantification approach to better define failure orientation and magnitude, improve our understanding of the failure kinematics, and better quantify the geometrical aspects of a slope failure.

ACKNOWLEDGEMENTS

The authors would like to acknowledge the financial support of *Transports Quebec* and the Natural Sciences and Engineering Research Council of Canada. The authors would also like to thank Pierre Dorval and François Bossé (*Service Géotechnique et Géologie - Transports Québec*) for providing airborne LiDAR survey data, pictures and technical advice. Finally, the authors are grateful to Michel Vallée and Gilles Bonin for providing easy mine site access.

REFERENCES

Abellan A, Jaboyedoff M, Oppikofer T, Vilaplana JM (2009) Detection of millimetric deformation using a terrestrial laser scanner: experiment and application to a rockfall event. Nat Hazards Earth Syst Sci 9:365–372. doi: 10.5194/nhess-9-365-2009

Abellan A, Calvet J, Vilaplana JM, Blanchard J (2010) Detection and spatial prediction of rockfalls by means of terrestrial laser scanner monitoring. Geomorphology 119:162–171. doi: 10.1016/ j.geomorph.2010.03.016

Abellan A, Vilaplana JM, Calvet J, Garcıa-Selles D, Asension E (2011) Rockfall monitoring by Terrestrial Laser Scanning—case study of the basaltic rock face at Castellfollit de la Roca (Catalonia, Spain). Nat Hazards Earth Syst Sci. doi: 10.5194/ nhess-11-829-2011

Abellan A, Oppikofer T, Jaboyedoff M, Rosser NJ, Lim M, Lato MJ (2014) Terrestrial laser scanning of rock slope instabilities. Earth Surf Process Landf 39:80–97. doi: 10.1002/esp.3493

ArcGIS (2010) Desktop Service Pack 5, ArcMAP v10.0

Beauchamp Y (1994) Retro analyse de l'instabilite de décembre 1993 à la paroi sud-Ouest de la rampe principale, LAB Chrysotile mine

Bonnaffe F, Jennette D, Andrews J (2007) A method for acquiring and processing ground-based lidar data in difficult-to-access outcrops for use in three-dimensional, virtual-reality models. Geosphere 3:501–510. doi: 10.1130/ges00104.1

Bye AR, Bell FG (2001) Stability assessment and slope design at sandsloot open pit, South Africa. Int J Rock Mech Min Sci 38:449–466. doi: 10.1016/s1365-1609(01)00014-4

Caduff R, Schlunegger F, Kos A, Wiesmann A (2015) A review of terrestrial radar interferometry for measuring surface change in the geosciences. Earth Surf Process Landf 40:208–228. doi: 10. 1002/esp.3656

Carrea D, Abellan A, Derron MH, Gauvin N, Jaboyedoff M (2012) Using 3D surface datasets to understand landslide evolution: from analogue models to real case study. In: Eberhardt E, Froese C, Turner K, Leroueil S (eds) Landslides and engineered slopes: protecting society through improved understanding. CRC Press, Boca Rotan, pp 575–579

CloudCompare V2 (2016) License: GNU GPL (General Public Licence) v. 2.7, Widows 64 bit. http://www.danielgm.net/cc. Accessed 3 Nov 2016

Corsini A, Borgatti L, Coren F, Vellico M (2007) Use of multitemporal airborne lidar surveys to analyse post-failure behaviour of earth slides. Can J Remote Sens 33:116–120. doi: 10.5589/m07- 015

Curtaz M, Ferrero AM, Roncella R, Segalini A, Umili G (2014) Terrestrial Photogrammetry and numerical modelling for the stability analysis of rock slopes in high mountain areas: aiguilles Marbrées case. Rock Mech Rock Eng 47:605–620. doi: 10.1007/ s00603-013-0446-z

Dick GJ, Eberhardt E, Cabrejo-Lievano AG, Stead D, Rose ND (2014) Development of an early-warning time-of-failure analysis methodology for open-pit mine slopes utilizing ground-based slope stability radar monitoring data. Can Geotech J 52:515–529. doi: 10.1139/cgj-2014-0028

Eberhardt E, Stead D (2011) Geotechnical instrumentation. In: Darling P (ed) SME mining engineering handbook, vol 1, 3rd edn. Society for Mining, Metallurgy, and Exploration, Englewood, pp 551–572

Eberhardt E, Bonzanigo L, Loew S (2007) Long-term investigation of a deep-seated creeping landslide in crystalline rock. Part II. Mitigation measures and numerical modelling of deep drainage at Campo Vallemaggia. Can Geotech J 44:1181–1199. doi: 10.1139/T07-044

Ferrero AM, Forlani G, Roncella R, Voyat HI (2009) Advanced geostructural survey methods applied to rock mass characterization. Rock Mech Rock Eng 42:631–665. doi:10.1007/s00603-008-0010-4

Froese CR, Moreno F, Jaboyedoff M, Cruden DM (2009) 25 years of movement monitoring on South Peak, Turtle Mountain: nderstanding the hazard. Can Geotech J 46:256–269. doi: 10.1139/t08-121

Fruneau B, Achache J, Delacourt C (1996) Observation and modelling of the Saint-Étienne-de-Tinée landslide using SAR interferometry. Tectonophysics 265:181–190. doi:10.1016/S0040-1951(96)00047-9

Gordon P, Charles T (2008) Terrestrial laser scanners. In: Shan J,Toth CK (eds) Topographic laser ranging and scanning principles and processing. CRC Press, pp 87–128. doi: 10.1201/9781420051438.ch3

Grenon M, Caudal P, Amoushahi S, Turmel D, Locat J (2016) Analysis of a large rock slope failure on the east wall of the LAB chrysotile mine in Canada: back analysis, impact of water infilling and mining activity. Rock Mech Rock Eng. doi: 10.1007/ s00603-016-1116-8

InnovMetric Software Inc. (2012) Polyworks v. 12.0.17, build 5761, 64 bit

Jaboyedoff M, Oppikofer T, Abellan A, Derron M-H, Loye A, Metzger R, Pedrazzini A (2012) Use of LIDAR in landslide investigations: a review. Nat Hazards 61:5–28. Doi: 10.1007/s11069-010-9634-2

Lato MJ, Diederichs MS, Hutchinson DJ, Harrap R (2012) Evaluating roadside rockmasses for rockfall hazards using LiDAR data: optimizing data collection and processing protocols. Nat Hazards 60:831–864. doi: 10.1007/s11069-011-9872-y

Lato MJ, Hutchinson DJ, Gauthier D, Edwards T, Ondercin M (2014) Comparison of airborne laser scanning, terrestrial laser scanning, and terrestrial photogrammetry for mapping differential slope change in mountainous terrain. Can Geotech J 52:129–140. doi: 10.1139/cgj-2014-0051

Michoud C, Abellan A, Derron M.H, Jaboyedoff M (2010) Review of techniques for landslide detection, fast characterization, rapid mapping and long-term monitoring. SafeLand deliverable 4.1. https://www.dropbox.com/s/q42p2ht4jop3rqq/2010%20SAFELAND_Deliverable_4.1.pdf?dl=0 . Accessed 3 Nov 2016

Monserrat O, Crosetto M (2008) Deformation measurement using terrestrial laser scanning data and least squares 3D surface matching. ISPRS J Photogramm Remote Sens 63:142–154. doi: 10.1016/j.isprsjprs.2007.07.008

Oppikofer T, Jaboyedoff M, Keusen H-R (2008) Collapse at the eastern Eiger flank in the Swiss Alps. Nat Geosci 1:531–535. http://www.nature.com/ngeo/journal/v1/n8/suppinfo/ngeo258_S1.html

Optech (2011) ILRIS 3D-ER, summary specification sheet. Optech, Ontario

Pesci A, Casula G, Boschi E (2011) Laser scanning the Garisenda and Asinelli towers in Bologna (Italy): detailed deformation patterns of two ancient leaning buildings. J Cult Herit 12:117–127

Prokop A, Panholzer H (2009) Assessing the capability of terrestrial laser scanning for monitoring slow moving landslides. Nat Hazards Earth Syst Sci 9(6):1921–1928. doi: 10.5194/nhess-9-1921-2009

Read J, Stacey P (2009) Guidelines for open pit slope design. CSIRO Publishing, Clayton

Squarzoni C, Delacourt C, Allemand P (2003) Nine years of spatial and temporal evolution of the La Valette landslide observed by SAR interferometry. Eng Geol 68:53–66. doi: 10.1016/S0013-7952(02)00198-9

Teza G, Galgaro A, Zaltron N, Genevois R (2007) Terrestrial laser scanner to detect landslide displacement fields: a new approach. Int J Remote Sens 28:3425–3446. doi: 10.1080/01431160601024234

Teza G et al (2008) Ground-based monitoring of high risk landslides through joint use of laser scanner and interferometric radar. Int J Remote Sens 29:4735–4756. doi: 10.1080/01431160801942227

Travelletti J, Oppikofer T, Delacourt C, Malet JP, Jaboyedoff M (2008) Monitoring landslide displacements during a controlled rain experiment using a long-range terrestrial laser scanning (TLS). Int. Arch. Photogramm. Remote Sens 37(part B5):485–490

Turmel D, Leblanc J, Locat J, Grenon M (2015) Établissement de scénarios d'accèlèration et de vitesse de grands glissements rocheux actifs: le cas de Black Lake. In: Proceedings of the 68th Canadian geotechnical conference, GeoQuébec, Québec. Paper 507

Woo K-S, Eberhardt E, Rabus B, Stead D, Vyazmensky A (2012) Integration of field characterisation, mine production and InSAR monitoring data to constrain and calibrate 3-D numerical modelling of block caving-induced subsidence. Int J Rock Mech Min Sci 53:166–178. doi: 10.1016/j.ijrmms.2012.05.008